

Multi-band, Multi-epoch Observations of the Transiting Warm Jupiter WASP-80b

Akihiko Fukui¹, Yui Kawashima², Masahiro Ikoma², Norio Narita^{3,4}, Masahiro Onitsuka⁴,
Yoshifusa Ita⁵, Hiroki Onozato⁵, Shogo Nishiyama^{3,6}, Haruka Baba⁴, Tsuguru Ryu⁴,
Teruyuki Hirano⁷, Yasunori Hori^{8,9}, Kenji Kurosaki², Kiyoe Kawauchi⁷,
Yasuhiro H. Takahashi^{3,10}, Takahiro Nagayama¹¹, Motohide Tamura¹², Nobuyuki Kawai¹³,
Daisuke Kuroda¹, Shogo Nagayama³, Kouji Ohta¹⁴, Yasuhiro Shimizu¹, Kenshi Yanagisawa¹,
Michitoshi Yoshida¹⁵, and Hideyuki Izumiura¹

afukui@oao.nao.ac.jp

ABSTRACT

WASP-80b is a warm Jupiter transiting a bright late-K dwarf, providing a good opportunity to extend the atmospheric study of hot Jupiters toward the lower temper-

¹Okayama Astrophysical Observatory, National Astronomical Observatory of Japan, Asakuchi, Okayama 719-0232, Japan

²Department of Earth and Planetary Science, Graduate School of Science, The University of Tokyo, 7-3-1 Bunkyo-ku, Tokyo 113-0033, Japan

³National Astronomical Observatory of Japan, 2-21-1 Osawa, Mitaka, Tokyo 181-8588

⁴The Graduate University for Advanced Studies, 2-21-1 Osawa, Mitaka, Tokyo 181-8588

⁵Astronomical Institute, Graduate School of Science, Tohoku University, 6-3 Aramaki Aoba, Aoba-ku, Sendai, Miyagi 980-8578, Japan

⁶Faculty of Education, Miyagi University of Education, Sendai, 980-0845, Japan

⁷Department of Earth and Planetary Sciences, Tokyo Institute of Technology, 2-12-1 Ookayama, Meguro-ku, Tokyo 152-8551

⁸Department of Astronomy and Astrophysics, University of California, Santa Cruz, CA 95064, USA

⁹Division of Theoretical Astronomy, National Astronomical Observatory of Japan, Osawa, Mitaka, Tokyo 1818588, Japan

¹⁰Ministry of Education, Culture, Sports, Science and Technology, Japan, 3-2-2, Kasumigaseki, Chiyoda-ku, Tokyo 100-8959, Japan

¹¹Department of Physics, Nagoya University, Furo-cho, Chikusa-ku, Nagoya 464-8602, Japan

¹²Department of Astronomy, Graduate School of Science, The University of Tokyo, and National Astronomical Observatory of Japan

¹³Dept. of Physics, Tokyo Institute of Technology, 2-12-1, Ookayama, Meguro, Tokyo, 152-8551, Japan

¹⁴Dept. of Astronomy, Kyoto University, Kitashirakawa-Oiwake, Sakyo, Kyoto, 606-8502, Japan

¹⁵Hiroshima Astrophysical Science Center, Hiroshima University 1-3-1, Kagamiyama, Higashi-Hiroshima, Hiroshima, 739-8526, Japan

ature regime. We report multi-band, multi-epoch transit observations of WASP-80b by using three ground-based telescopes covering from optical (g' , R_c , and I_c bands) to near infrared (NIR; J , H , and K_s bands) wavelengths. We observe five primary transits, each of which in three or four different bands simultaneously, obtaining 17 independent transit light curves. Combining them with previous works, we find that the observed transmission spectrum is largely consistent with both a solar-abundance and thick-cloud atmospheric models at $1.7\text{-}\sigma$ discrepancy level. On the other hand, we find a marginal spectral rise in optical region compared to NIR region at $2.9\text{-}\sigma$ level, which possibly indicates the existence of haze in the atmosphere. We simulate theoretical transmission spectra for a solar-abundance but hazy atmosphere, finding that a model with equilibrium temperature of 600 K can explain the observed data well, having the discrepancy level of $1.0\text{ }\sigma$. We also search for transit timing variations, but find no timing excess larger than 50 s from a linear ephemeris. In addition, we conduct 43-day-long photometric monitoring of the host star in the optical bands, finding no significant variation of the stellar brightness. Combined with the fact that no spot-crossing event is observed in the five transits, our results confirm previous findings that the host star appears quiet as for spot activities, despite the indications of strong chromospheric activities.

Subject headings: planetary systems — planets and satellites: atmospheres — planets and satellites: individual(WASP-80b) — stars: individual(WASP-80) — techniques: photometric

1. Introduction

It is now well known that exoplanets have diverse orbits reflecting diverse planetary origins and various migration mechanisms. To explore such planetary formation histories, unveiling their atmospheric compositions is important, because they can be affected by the environments where they were born. For example, the relative abundances of carbon- and oxygen-bearing molecules in planetary atmospheres are closely related to the environment of surrounding disk gas (e.g., Öberg et al. 2011; Madhusudhan 2012).

If an exoplanet has a transiting orbit, the planetary atmospheric composition can be examined by measuring transit and secondary-eclipse depths as a function of wavelength, which are referred to as transmission and emission spectroscopy, respectively. So far, several molecular features, such as H_2O , CH_4 , CO_2 , and CO , have been detected through these techniques in several hot Jupiters (e.g., Barman 2007; Tinetti et al. 2007, 2010; Swain et al. 2008, 2009; Grillmair et al. 2008; Swain et al. 2010; Snellen et al. 2010; Wakeford et al. 2013), although some of the detections are still in dispute (e.g. Sing et al. 2009; Gibson et al. 2011; Swain et al. 2014). On the other hand, flat or featureless transmission spectra have also been observed in a number of exoplanets, ranging from hot Jupiters, e.g., HD 189733b, WASP-12b, HAT-P-32b, and HAT-P-1b (Pont et al. 2008; Sing et al.

2013; Gibson et al. 2013; Nikolov et al. 2014) to super-Earths/Neptunes, e.g., GJ1214b and GJ436b (Kreidberg et al. 2014; Knutson et al. 2014a), raising the possibility of the existence of floating small particles (aerosols) in their atmospheres as strong opacity sources. Such aerosols obscure or interfere with other atmospheric features (Fortney 2005), preventing us from properly measuring the relative abundances of fundamental molecules such as H_2O , CH_4 , CO_2 , and CO . Therefore, understanding the nature of aerosols is crucial to explore planetary formation histories through their atmospheres.

Understanding the behaviors of aerosols is more important for cooler atmospheres. In an atmosphere with temperature below $\sim 1,000\text{K}$, CH_4 becomes a major carbon carrier instead of CO . When such a CH_4 -rich atmosphere is irradiated by UV fluxes, hydro-carbon haze particles (tholins) can be produced via photochemical processes. Indeed, such tholin hazes can be seen in CH_4 -existing planets and satellites in our Solar system (e.g., Uranus and Titan). However, few exoplanets that have low-temperature atmospheres have been investigated to date. This is notable in gas giants¹, because transiting gas giants around late-type (low-temperature) stars are rare (e.g., Johnson et al. 2012).

In this context, recently, a transiting Jovian planet WASP-80b was discovered around a nearby (60 ± 20 pc) late-K dwarf (Triaud et al. 2013). This planet has several attractive points for studying its atmosphere. First, the planet has an equilibrium temperature of ~ 800 K or less (assuming albedo is >0.1), which is one of the lowest temperatures among those of transiting Jovian planets around bright ($J < 10$) host stars. Second, the host star shows strong chromospheric activities (Triaud et al. 2013; Mancini et al. 2014), possibly causing active photochemical reactions in the planetary atmosphere that might produce abundant tholin particles. Lastly, the planet shows the second largest transit depth ($\sim 2.9\%$) following Kepler-45b ($\sim 3.2\%$) among the known transiting planets, allowing us to measure the transit depth with relatively high precision. Therefore, WASP-80b offers a good opportunity to extend the atmospheric study toward the low-temperature regime, and test the photochemical reactions of hydro-carbons in an exoplanetary atmosphere.

Recently, Mancini et al. (2014) conducted optical-to-near-infrared simultaneous observations for a transit of WASP-80b by using the GROND instrument on the MPG/ESO 2.2-m telescope (g' , r' , i' , z' , J , H , and K bands) and the 1.54-m Danish telescope (I band), reporting a flat transmission spectrum within the observational uncertainties. However, because the data are also consistent with a model spectrum assuming a solar-abundance atmosphere, further observations are needed to characterize its atmosphere. Furthermore, they omitted the H - and K -band observational data in their discussion of the spectrum due to relatively poor quality, leaving large room for improvement especially in the NIR regions.

In this paper, we report multi-band, multi-epoch transit observations of WASP-80b. We ob-

¹We note that atmospheres of low-temperature gas giants in wide orbits have recently been investigated by direct imaging (e.g., Kuzuhara et al. 2013).

served five primary transits, each of which in three or four different bands, using three ground-based telescopes at two observatories. Such multi-band and multi-epoch observations are quite useful not only to reduce statistical uncertainties but also to check systematics in measured parameters, especially for ground-based observations, which often suffer from unknown systematics and/or lack of full-transit coverages. We also report 43-day-long photometric observations of the host star WASP-80 in optical three bands, to monitor its intrinsic variability. This is important, because if the stellar brightness significantly varies from transit to transit due to such as star-spot appearing/vanishing, the observed transmission spectrum, or practically star-to-planet radius ratio R_p/R_s , can be biased (e.g. Pont et al. 2008).

The rest of this paper is organized as follows. We describe our observations in Section 2. The methods of reduction and analysis of the observed data are shown in Section 3. The transit timings, stellar variability, and atmospheric properties of the WASP-80 system are discussed in Section 4. Finally, we summarize this paper in Section 5.

2. Observations

2.1. Transit Observations with IRSF/SIRIUS

We observed three primary transits of WASP-80b with the Simultaneous Infrared Imager for Unbiased Survey (SIRIUS, Nagayama et al. 2003) camera mounted on the Infrared Survey Facility (IRSF) 1.4 m telescope in South African Astronomical Observatory on 2013 July 16, August 22, and October 7 (UT). SIRIUS has three detectors, each consists of $1k \times 1k$ pixels with a pixel scale of $0''.45 \text{ pixel}^{-1}$, enabling to obtain J -, H -, and K_s -band images simultaneously with a field of view (FOV) of $7'.7 \times 7'.7$. During each observation, we defocused stellar images so that the full-width at half maximum (FWHM) of stellar point spread function (PSF) was 14–17 pixels on July 16 and October 7, and 9.5–12 pixels on August 22, in order to improve photometric precision. In addition, we activated a software which corrects tracking errors by calculating the stellar positional shift on the just-obtained J -band image and feeding it back to the telescope. The exposure time was set to 10 s on July 16 and August 22, and 15 s on October 7. The weather was photometric without any thin cloud passing for the three nights. We observed full transit including pre- and post-transit parts on July 16 and October 7, however, we discarded the data before 22:47 on July 16 (UT) because of an accidental drift of the stellar position on the detector that causes uncorrectable systematic errors on photometry. The pre-transit part on August 22 was not observed due to interference with another observational program. In the lower-left panel in Figure 1–3, we show the air-mass change (top) and stellar positional change along x and y directions on the J -band detector (bottom) during the respective observations. An observing log is shown in Table 1.

2.2. Transit Observations with OAO188cm/ISLE and MITSuME

We observed two primary transits of WASP-80b by simultaneously using two instruments at Okayama Astrophysical Observatory (OAO) on 2013 August 13 and September 22 (UT); one is the NIR imaging and spectroscopic instrument ISLE (Yanagisawa et al. 2006, 2008) mounted on the 188-cm telescope and the other is a multi-color imager mounted on the 50-cm telescope which is one of Multicolor Imaging Telescopes for Survey and Monstrous Explosions (MITSuME, Kotani et al. 2005; Yanagisawa et al. 2010).

ISLE has a $1\text{k} \times 1\text{k}$ HAWAII-1 array having a pixel scale of $0''.25 \text{ pixel}^{-1}$ and a FOV of $4'.5$ on a side. We used J -band filter and set the exposure time to 45 s on both nights. We defocused stellar images so that the FWHM of stellar PSF was 23–27 pixels. In addition, we activated a hybrid auto-guiding system (Fukui et al. 2013), which consists of an off-axis auto-guiding camera to correct telescope’s tracking errors in real time, and a software which corrects a gradual drift of the origin of the auto-guiding camera with respect to the ISLE detector by calculating the shift of stellar positions on the ISLE images.

The multi-color imager mounted on the MITSuME telescope consists of three $1\text{k} \times 1\text{k}$ CCDs, enabling to obtain g' -, R_c -, and I_c -band images simultaneously. Each CCD has a pixel scale of $1''.5 \text{ pixel}^{-1}$, providing a FOV of $26'$ on a side. We slightly defocused the stellar images so that the FWHM of PSF was 1.2–2.5 pixels. We also activated a software which corrects the stellar positional shift on the I_c -band detector soon after each exposure. The exposure time was set to 30 s on both nights.

The weather was mostly photometric on both nights, while some thin clouds passed at the beginning of the observation on September 22, which results in large flux drops especially in optical bands; we discarded these data from the analysis in the rest of this paper. In the lower-left panel in Figure 4 and 5, we show air-mass change (top) and stellar positional change along x and y directions on the ISLE (middle) and MITSuME/ I_c -band (bottom) detectors during the respective observations. An observing log is compiled in Table 1.

2.3. Photometric Monitoring of Stellar Variability with MITSuME

In order to check the intrinsic variability of the host star WASP-80 around the period of our transit observations, we conducted out-of-transit observations on 14 nights spanning 43 days from 2013 August 10 to 2013 September 22, by using the 50-cm MITSuME telescope in g' , I_c , and R_c bands. All the settings were the same as the transit observations described in the previous section. The observations were conducted for 1–2 hours on each night, and totally about 1700 images were gathered for each band.

3. Analysis

3.1. Data Reduction

All the observed images are dark-subtracted and flat-fielded in a standard manner. The flat-field images are created from dozens of twilight flat images that were obtained before and after each observation for the SIRIUS and MITSuME data, and from a hundred of dome-flat images that were taken on each observing night for the ISLE data. After that, aperture photometry is performed for the target and several (for SIRIUS and ISLE) or dozens (for MITSuME) of bright stars spread on the reduced images, by using a customized tool with constant-aperture-radius mode (Fukui et al. 2011). The target flux is divided by the sum of the fluxes of a selected number of bright stars (comparison stars) to produce a relative light curve.

The time for each data point is assigned as the mid time of exposure in the time system of Barycentric Julian Day (BJD) based on Barycentric Dynamical Time (TDB), which is converted from Julian Day (JD) based on Coordinated Universal Time (UTC), recorded on the FITS header, via the code of Eastman et al. (2010).

3.2. Preparation of Transit Light Curves

In order to optimize the set of comparison stars and aperture radius for each instrument, filter, and transit (each dataset), we produce a number of trial light curves for each dataset by changing combination of comparison stars, as well as changing aperture radius with a step size of 0.5 pixel (for MITSuME) or 1 pixel (for others). Then, we fit the individual trial light curves with a transit-plus-baseline model to select the best light curve so that the root mean square (RMS) of the residual light curve is minimum. For the light curve model, we use the following functions,

$$F = k_0 \times 10^{-0.4\Delta m_{\text{corr}}} \times F_{\text{tr}}, \quad (1)$$

$$\Delta m_{\text{corr}} = \sum_{i=1} k_i X_i, \quad (2)$$

where F is the relative flux, F_{tr} is the transit light-curve model, $\{\mathbf{X}\}$ are variables for the baseline function, and $\{\mathbf{k}\}$ are coefficients. For the variables $\{\mathbf{X}\}$, we tentatively use $\{t, z\}$, where t is time and z is air mass. For the transit model F_{tr} , we use the analytic formula given by Ohta et al. (2009), which is equivalent with that of Mandel & Agol (2002) when using the quadratic limb-darkening law. The transit parameters we use are the mid transit time T_c , the planet-star radius ratio R_p/R_s , the semi-major axis normalized by the stellar radius a/R_s , the orbital inclination i_{orb} , and the quadratic limb-darkening coefficients u_1 and u_2 . Among these parameters, T_c , R_p/R_s and u_1 are let free, while a/R_s and i_{orb} are fixed at the values derived from Mancini et al. (2014), namely, 12.6119 and 88.91 deg, respectively. We also fix u_2 at the theoretical values for a star with $\log g=4.5$ and $T_{\text{eff}}=4100$ K for respective filters, adopted from Claret et al. (2012), namely, 0.109, 0.191, 0.225, 0.223, 0.267, 0.241 for g' , R_c , I_c , J , H , and K_s , respectively. A circular orbit,

with the orbital period of $P = 3.06786144$ days adopted from Mancini et al. (2014), is assumed. The individual light curves are fitted by the AMOEBA algorithm (Press et al. 1992) to find the one which gives the minimum RMS value, by iteratively eliminating $>4\sigma$ outliers. In Table 2, we summarize the number of selected comparison stars and the selected aperture radius for all datasets. The selected light curves are shown in the left-upper panels in Figure 1–5, where 10-min-binned data are also shown for eye guide. We note that there exists a fainter neighboring star ($\Delta B=2.8$ and $\Delta K_s=4.0$) which is separated from WASP-80 by $8''.9$; we confirm that with the selected aperture radii the flux contamination from the fainter star is negligible for all the datasets.

3.3. Selection of Baseline Models

After preparing the light curves, we select the best-describing baseline model, i.e., which variables should be included in $\{\mathbf{X}\}$ in Equation (2), for each light curve. To do so, first, we fit each light curve with Equation (1) and (2) letting T_c , R_p/R_s , u_1 , and a/R_s be free while fixing others, by changing the set of variables $\{\mathbf{X}\}$. The set of variables are chosen from t , z , t^2 , Δx , and Δy , where Δx and Δy are the relative stellar displacement along the x and y directions, respectively, on the detectors. Next, we evaluate the Bayesian information criteria (BIC; Schwarz 1978) for each baseline model; The BIC value is given by $\text{BIC}=\chi^2 + k \ln N$, where k is the number of free parameters and N is the number of data points. Finally, we select the best baseline model such that the BIC value is minimum.

This procedure works well for all the light curves, except for the J - and H -band light curves obtained on 2013 August 22. For these two light curves, we find that the fittings with the minimum-BIC models, namely $\{\mathbf{X}\}=\{t, t^2\}$ for both of the two, derive inconsistent a/R_s values with that derived from Mancini et al. (2014), although for all the other light curves the comparable fittings derive consistent a/R_s values, largely within their uncertainties (see Figure 6). The two exceptional light curves are lack of pre-transit part; in such a case, incorrect baseline models can incidentally fit the data well. If this is the case, the derived R_p/R_s value, which is what we want to measure, could be shifted from the true value. In fact, the respective R_p/R_s values for the J - and H -band light curves on August 22 are significantly larger than those for the same-band light curves on October 7 (see the corresponding panels in Figure 6), in which before and after the transit are both well covered. For the two exceptions, we alternatively find that a simpler baseline model of $\{\mathbf{X}\} = \{z\}$ can fit them giving consistent a/R_s values with the Mancini et al.’s one as well as consistent R_p/R_s values with the same-band light curves on October 7 (denoted as open circles in Figure 6), while the BIC differences between $\{\mathbf{X}\} = \{z\}$ and $\{t, t^2\}$ for the J - and H -band light curves are 18.8 and 34.1, respectively. For the above reasons, we choose $\{\mathbf{X}\} = \{z\}$ as a best-describing baseline model for these two light curves. We note that it is not likely that a/R_s and R_p/R_s have changed over time, because fitting to the K_s -band light curve on the same night with the minimum-BIC model gives a consistent a/R_s value with the Mancini et al.’s one. In Table 2, we summarize the selected sets of variables $\{\mathbf{X}\}$ for the respective light curves.

We also note that even for the other light curves, there can be several baseline models that give similar BIC values to the minimum one, potentially causing systematic errors on R_p/R_s depending on which baseline we select. To see the impact of this possibility, we also plot the R_p/R_s and a/R_s values for the baseline models that give the BIC difference with respect to the minimum-BIC model (ΔBIC) of less than five, in Figure 6. As a result, the R_p/R_s and a/R_s values for similar-BIC models (filled circle, triangle, and square are for the minimum, second-, and third-minimum BIC models, respectively) are close to each other compared to their uncertainties, implying that the systematics on R_p/R_s due to different baseline models are small.

After the baseline-selection process, we rescale the flux uncertainties in each light curve such that the reduced χ^2 of the transit-plus-baseline-model fit becomes unity. In addition, we further rescale these uncertainties by the so-called β factor (Winn et al. 2008) taking red noises into account. The β factor is defined as $\sigma_{N,\text{obs}}/\sigma_{N,\text{exp}}$, where $\sigma_{N,\text{obs}}$ is the standard deviation of the residual light curve binned by N data points into M bins, and $\sigma_{N,\text{exp}} \equiv \sigma_1 \sqrt{M/N(M-1)}$ is the expected standard deviation for the binned residual light curve assuming that the un-binned residuals with the standard deviation of σ_1 are dispersed in a gaussian distribution. We take the median value of β calculated for $N = 4$ to 15 for each light curve. The calculated β values are summarized in Table 2.

3.4. MCMC analysis

To properly derive the R_p/R_s values and their uncertainties for the respective datasets, we perform the Markov Chain Monte Carlo (MCMC) analysis for each transit by using a customized code (Narita et al. 2007, 2013). In this analysis, all the light curves involved in one transit are simultaneously analyzed, treating i_{orb} , a/R_s , and T_c as common parameters, whereas R_p/R_s , u_1 , u_2 , and $\{\mathbf{k}\}$ as independent parameters for the respective light curves. Here, $\{\mathbf{k}\}$ are the coefficients corresponding to the variables $\{\mathbf{X}\}$ selected in the previous section. As the same way in Section 3.2, we fix i_{orb} and a/R_s at the values from Mancini et al. (2014), and fix u_2 at the theoretical values for the respective filters; we let the other adjustable parameters be free. The reason for fixing the i_{orb} and a/R_s values at the Mancini et al.’s ones is that these parameters are correlated with R_p/R_s , and varying them would cause systematic offset on measured R_p/R_s , which is what we aim to compare, including the ones from Mancini et al., in different bands (see Section 4.1). We start the MCMC procedure with the best-fit parameters determined by the AMOEBA algorithm, using their $1\text{-}\sigma$ uncertainties as the widths of gaussian jump functions for updating MCMC steps. We perform 10 sequential MCMC runs with 10^6 chained steps in each run, updating the best-fit parameters and their $1\text{-}\sigma$ uncertainties. To wait for convergence, we discard the first five MCMC runs. The final median values and $1\text{-}\sigma$ uncertainties of the respective parameters are calculated from the merged posterior-probability distributions from the last five MCMC runs.

The resultant parameters are summarized in Table 3. The final light-curve models are displayed as solid lines in the upper-left panels in Figure 1–5, as well as the baseline-corrected light curves

and residual light curves are shown in the upper-right and lower-right panels, respectively, in the same figures. We note that no apparent spot-crossing event is seen in any of the five transits.

3.5. Photometric Monitoring Data

For the 43-day-long photometric monitoring data gathered by the MITSuME telescope, we perform aperture photometry in the same way as done in Section 3.1 and 3.2. After eliminating the data points fallen in any transit events, we correct the systematics on the respective light curves by fitting them with Equation (1) and (2) fixing $F_{\text{tr}}=1$ and using $\{\mathbf{X}\}=\{z, \Delta x, \Delta y\}$. The resultant light curves with nightly-binned data points are shown in Figure 7, in which the error bars are calculated as RMS of the un-binned data on each night divided by the number of data points.

4. Discussion

4.1. Atmospheric Properties

In this section, we discuss the dependence of R_p/R_s on wavelength that could arise from the atmospheric properties of WASP-80b. In Figure 9, we plot the observed R_p/R_s values derived in Section 3.4 as a function of wavelength, along with those derived by Mancini et al. (2014). At each band, the measured values from different transits are consistent with each other within $2\text{-}\sigma$ uncertainties. Especially in the J band, we have now a total of six observations of R_p/R_s including the one from Mancini et al. (2014), and they are mostly well consistent with each other, indicating the correctness of our methodology and the smallness of systematics. We note that the effect of stellar intrinsic variability on measured R_p/R_s is negligible, as will be discussed in Section 4.3.

In order to search for atmospheric features in the observed R_p/R_s spectrum, first, we compare the overall observed data with two possible model spectra; one is from an atmospheric model with the solar abundances and the other is from an atmospheric model with opaque clouds. For the former model, we simulate the model spectrum assuming a solar-abundance atmosphere and the temperature of 800 K, which corresponds to the equilibrium temperature with albedo of 0.1 (Triaud et al. 2013), in the way described in Appendix; for the latter model, we approximate it simply as a flat line assuming that the atmosphere is thoroughly opaque in the wavelength range from optical to NIR. Note that our motivations for comparing with the cloudy model come from the fact that flat transmission spectra compatible with the presence of thick-cloud layers have been recently observed for several other low-temperature exoplanets such as GJ1214b (Kreidberg et al. 2014) and GJ436b (Knutson et al. 2014b), as well as the fact that Mancini et al. (2014) reported that their observed spectrum of WASP-80b is consistent with a flat line. We then fit the two model spectra to the data; for both cases, the number of free parameters is one: the radius of planetary disk that blocks the incident stellar radiation completely, R_0 . In the fitting process, we create a

theoretical R_p/R_s spectrum for each R_0 using the Equation (A2) and the fixed R_s value of $0.63 R_\odot$ (Triaud et al. 2013), and integrate the spectrum over each filter’s pass band to compare it with the observational data. The best-fitted models for the solar-abundance atmosphere and the cloudy atmosphere are shown respectively by the solid cyan and dashed grey lines in Figure 9. As a result, we find that the solar-abundance and cloudy models give the minimum- χ^2 values of 35.4 and 34.7, respectively, for the degrees of freedom (dof) of 25. These values mean that the two models are both largely consistent with the data at the discrepancy level of 1.7σ . When we discard the MITSuME data, which were obtained with a relatively small-aperture telescope and might contain relatively large unknown systematics, the solar-abundance and cloudy models fit the remaining data with $\chi^2/\text{dof}=24.3/19$ and $22.7/19$, respectively, reducing the discrepancy levels to 1.3 and 1.1σ . Therefore, we cannot rule out these two models from the current observational data.

On the other hand, we also find that the observed R_p/R_s in the optical region is marginally larger than that in the NIR region; the weighted mean of observed R_p/R_s in the optical ($\lambda < 1\mu\text{m}$) and NIR ($\lambda > 1\mu\text{m}$) regions are 0.17193 ± 0.00041 and 0.17029 ± 0.00039 , respectively, having a $2.9\text{-}\sigma$ discrepancy, while the discrepancy reduces to 2.0σ without the MITSuME data. As discussed in Introduction, because the equilibrium temperature of WASP-80b is about 800 K or less, photochemically produced hydro-carbon haze like tholin may exist in the atmosphere (e.g. Fortney et al. 2013). If so, the observed spectral rise in the optical region could be explained by the existence of tholin haze in the planetary atmosphere.

Motivated by this possibility, we model the transmission spectrum of a hazy atmosphere with the solar abundances and compare it with the observed data. The haze layer is characterized by four parameters that include the particle size a_{haze} , the number density n_{haze} , and the pressures at the top and bottom of the haze layer, which are denoted by P_{top} and P_{bot} , respectively. Values of P_{top} and P_{bot} are chosen in the way described in Appendix; In the case of GJ1214b, the way of choice is confirmed to yield values of P_{top} and P_{bot} that are consistent with the result from Morley et al. (2013). We assume $a_{\text{haze}} = 0.04 \mu\text{m}$, which is the typical size of haze particles in Titan’s atmosphere (Tomasko et al. 2009). We then search for the best-fit hazy model by changing n_{haze} every one order of magnitude from 10 to $1 \times 10^6 \text{ cm}^{-3}$, as well as letting R_0 be free. As a result, we find that $n_{\text{haze}} = 1 \times 10^4 \text{ cm}^{-3}$ gives the minimum- χ^2 value of 29.3 with $\text{dof} = 24$ (in this case, the number of free parameters is two) for temperature of 800 K, which means that the discrepancy level is 1.3σ . A comparable fit to the data without the MITSuME data gives $\chi^2/\text{dof} = 22.7/18$, or 0.99σ . These values are slightly better than those for the above two models of the haze-free solar-abundance atmosphere and the cloudy atmosphere.

In reality, however, we may have to consider temperature lower than 800 K. The 800 K corresponds to the globally-averaged equilibrium temperature of WASP-80b with albedo of 0.1. Since WASP-80b is likely to be tidally locked, the limb of the planetary disk that we observe may be much cooler than 800 K, provided the atmospheric heat redistribution is inefficient. Also, the high-altitude haze may block incident stellar flux from reaching the deep atmosphere. Thus, we consider 600 K, as an example of a moderately warm atmosphere, to simulate the transmission

spectrum, which is shown by the dotted magenta line in Fig. 9. In this case, the best-fit model (with $n_{\text{haze}} = 1 \times 10^4 \text{ cm}^{-3}$) results in the χ^2/dof of 26.8/24, giving the discrepancy level of only 1.0 σ . These statistical values decrease to $\chi^2/\text{dof}=19.5/18$ and 0.92 σ for the case without the MIT-SuME data. These results indicate that the hazy atmosphere model with temperature of 600 K is rather consistent with the observed data, relative to the above three models. In contrast, we also find that the haze-free solar-abundance atmosphere of 600 K yields a large χ^2/dof of 44.2/25 and 29.7/19 for the data with and without the MITSuME data, respectively. In Table 4, we summarize the statistical results of the model fittings discussed above.

More extensive search for the best-fit model is beyond the scope of this study, because the observed data have too large uncertainties and too low wavelength resolutions. Also, we need more detailed treatment concerning the role of haze on the atmospheric temperature and the heat redistribution in the atmosphere, which will be future studies. Nevertheless, we confirm that at least one atmospheric model with haze can explain the observed data well. Thus, the relatively large R_p/R_s in the optical region detected by our observation has raised another possibility of the presence of haze in the atmosphere. Higher-precision and higher-wavelength-resolution observations are desired to further shed light on this possibility.

4.2. Transit Timings

Thanks to the multi-epoch observations, we are able to refine the transit ephemeris as well as search for transit timing variations (TTVs) that would be caused by additional perturbing planets (e.g., Holman et al. 2010). Especially the latter is of interest, because warm Jupiters may have higher probability of having TTV-causing neighboring planets compared to hot Jupiters, most of which are known to be solitary (e.g., Steffen et al. 2012).

Using the mid-transit times of the five transits measured in Section 3.4 as well as those from the previous works, we refine the transit ephemeris of WASP-80b as $T_c (\text{BJD}_{\text{TDB}}) = 2456125.417574 (86) + 3.06785952 (77) \times E$, where E is the relative transit epoch and the numbers in parentheses indicate the uncertainties written to the last two significant digits. The residuals of the observed transit timings from the above ephemeris are shown in Figure 8. The χ^2 value for the linear fit is 59.0 for the degrees of freedom of 11, indicating that a liner function does not fit the data well. This in principle could be due to perturbations from an additional object in the planetary system, however, could be due to small-number statistics and/or unknown systematics as well (e.g. Maciejewski et al. 2013; Barros et al. 2013; Southworth et al. 2012; Hoyer et al. 2012). In addition, we can not see any plausible periodicity nor large amplitude exceeding ~ 50 s that are usually seen in the detection cases (e.g. Mazeh et al. 2013). Therefore, we do not claim a detection of TTVs due to a third body at this time.

4.3. Stellar Variability

To check the existence/absence of stellar intrinsic variability that causes systematic offsets on the observed R_p/R_s , we investigate the 43-days-long light curves created in Section 3.5. The χ^2 values of the 14 nightly-binned data with respect to a constant fit are 212.7, 181.8, and 137.4 for g' , R_c , and I_c bands, respectively, suggesting that the host star’s brightness could significantly vary over time. However, the data points in different bands are not correlated each other, with the correlation coefficients between I_c and R_c , R_c and g' , and g' and I_c are -0.26, 0.29, -0.32, respectively. This fact indicates that the observed dispersions are due to systematics rather than astrophysical origin. In addition, no periodic variation nor linear trend can be seen in any of the three light curves. Therefore, we do not detect any star-spot-induced periodic variability with the semi-amplitude larger than 0.25%, 0.3%, and 0.7% for I_c , R_c , and g' bands, respectively, during the observed period range of 43 days. And even if the observed dispersions were astrophysical origin, the maximum variability of 0.7% in g' band would change the observed R_p/R_s values by only 0.07%, or 0.0001 in units of R_p/R_s , which is negligible compared to the uncertainties of R_p/R_s .

The non detection of significant stellar variability is in line with the report of Triaud et al. (2013), who did not detect >1 mmag rotational variability from wide-band ($V+R$) photometric data of the WASP transit survey as well as from multi-epoch observations with a 60-cm telescope. We therefore confirm from the multi-band observations that the host star WASP-80 does not show spot-induced large ($>$ a few mmag) periodic variations. In addition, so far no spot-crossing event has been observed during any of the transits observed in this work nor in the previous works (nine transits in total), implying that not so many/large spots are distributed in the stellar surface. On the other hand, Triaud et al. (2013) pointed out that the star could be young because of its high projected-stellar rotational velocity ($v\sin i_s = 3.55 \pm 0.33$ km s $^{-1}$), depletion of lithium, and the presence of Ca $H+K$ emission, although there is also an anti-evidence that the galactic dynamical velocities are low. In addition, Mancini et al. (2014) detected strong Ca $H+K$ emission lines which indicate a strong magnetic activity of the star. If the star is truly young and active, the star would be expected to be heavily spotted. If so, the possible scenario would be either that a lot of small spots are widely distributed on the stellar surface (Mancini et al. 2014), or that the stellar inclination i_s is very small such that the polar region of the stellar surface is always facing to us. Especially, the latter idea is consistent with the fact that the projected spin-orbit angle β was measured as significantly non-zero value ($\pm 75^\circ \pm 4$), assuming $V\sin i_s = v\sin i_s$, where $V\sin i_s$ and $v\sin i_s$ are the projected stellar-rotation velocities measured from the Rossiter-McLaughlin effect and spectral equivalent width, respectively (Triaud et al. 2013). In this case, the star should be rotating very fast, possibly less than a few days. Photometric monitoring of the star with much higher precision may help to measure the rotational period and test this possibility.

5. Summary

In this paper, we report multi-band, multi-epoch observations of the transiting warm Jupiter WASP-80b, which is suitable for studying low-temperature atmospheres of exoplanets. We observed five primary transits of this planet using three instruments and seven different filters. Consequently, we obtained 17 independent transit light curves in six bands covering from optical to near infrared (NIR) wavelength regions. We compare the observed R_p/R_s values including those from previous works with two model spectra, one is from a solar-abundance atmospheric model and the other is from a thick-cloud one. As a result, we find that the observed data are largely consistent with both the two models at 1.7σ . Therefore, we cannot rule out these two models from the current observations.

On the other hand, we also find that the observed R_p/R_s in optical is marginally larger than that in NIR at $2.9\text{-}\sigma$ significance, possibly indicating the existence of haze in the planetary atmosphere. We compare the data with theoretical spectra for a solar-abundance but hazy atmosphere, and find that a model with the equilibrium temperature of 600K fits the data at 1.0σ , indicating that the hazy atmospheric model can explain the observed data well. To confirm/reject this possibility, further higher-precision and higher-spectral-resolution observations are required.

We also search for transit timing variations from totally 13 timing data (9 transits) from this work and previous works. As a result, we do not find any periodic timing variation nor timing excess larger than 50 s from a linear ephemeris, meaning that there is no considerable sign of additional neighboring planet at this time.

In addition, we conducted 43-day-long photometric monitoring of the host star in g' , R_c , and I_c bands, resulting in non detection of significant brightness variations. Combining with the fact that no spot-crossing event is observed in the five transits, we confirm the findings of Triaud et al. (2013) and Mancini et al. (2014) that the host star appears quiet as for spot activities, despite the indications of strong chromospheric activities. This weird consequence could be explained if the host star has a polar-on orbit. This possibility can be tested by measuring the stellar rotational period by monitoring the stellar brightness with much higher precision.

A. Outline of Transmission Spectrum Modeling

The theoretical value of the transit radius at wavelength λ , $R_{p,\text{th}}(\lambda)$, is calculated as

$$\left[\frac{R_{p,\text{th}}(\lambda)}{R_s} \right]^2 = \frac{1}{\pi R_s^2} \int_0^{R_s} \left\{ 1 - e^{-\tau(r,\lambda)} \right\} \cdot 2\pi r dr, \quad (\text{A1})$$

where R_s is the host star's radius, r is the planetocentric distance and τ is the chord optical thickness (see e.g. Kurosaki et al. 2014). We assume that the planetary disk of radius R_0 blocks

the incident stellar radiation completely, which means

$$\{R_{\text{p,th}}(\lambda)\}^2 = R_0^2 + \int_{R_0^2}^{R_s^2} \left\{1 - e^{-\tau(r,\lambda)}\right\} dr^2. \quad (\text{A2})$$

In this study, we define R_0 as the planetocentric distance at which the atmospheric pressure is 10 bar. Since the pressure profile in the atmosphere is unknown in advance, we treat R_0 as a free parameter in searching for the best-fit model by χ^2 analysis. The atmosphere is assumed to be in hydrostatic equilibrium and isothermal for simplicity; $R_{\text{p,th}}$ is known to be less sensitive to atmospheric pressure-temperature profile (Miller-Ricci & Fortney 2010; Howe & Burrows 2012). We also assume that the element abundances are radially constant, and calculate chemical-equilibrium molar fractions of molecules at each altitude with the Gibbs free energy data from NIST-JANAF Thermochemical Tables (Chase 1998). We determine the element abundance ratios of solar-abundance atmosphere from Lodders (2003).

As for the sources of radiative extinction, we consider line absorption by H_2 , H_2O , CH_4 , CO , CO_2 , NH_3 , N_2 , Na , and K gases, and collision-induced absorption by H_2 - H_2 and H_2 - He for the solar-abundance model, and additionally, scattering by haze particles for the hazy atmospheric models. We take line data for those gaseous molecules except Na and K from HITRAN2012 (Rothman et al. 2013) and those for Na and K from Kurucz (1992), and calculate the absorption cross sections for those gases with the Voigt profile (e.g., Goody & Yung 1989). In practice, we use the geometric mean of the wavelength-dependent cross sections over a range with wavenumber width of 3.3 cm^{-1} . The cross sections due to the collision-induced absorption are taken from HITRAN2012.

For haze particles, we assume hydrocarbon haze, which is often called tholin. Taking its complex indices of refraction from Khare et al. (1984), we calculate its extinction coefficients based on the Mie theory, using HITRAN-RI program in HITRAN2012. The haze layer is characterized by four parameters that include the particle size a_{haze} , the number density n_{haze} , the pressures at the top and bottom of the haze layer which are denoted by P_{top} and P_{bot} , respectively. Hydrocarbon haze is usually produced from CH_4 . CH_4 is the major C-bearing molecule in the lower atmosphere, while CO is dominant in the upper atmosphere. Thus, hydrocarbon haze should appear around the altitude where CH_4 changes to CO . According to recent simulations of photochemistry in the atmosphere of GJ1214b by Morley et al. (2013), the precursor molecules such as C_2H_2 forms at such an altitude and is distributed in the region that ranges over 1-2 orders of magnitude in pressure. In this study, we calculate the equilibrium composition to find the altitude at which CH_4 is equal in mole fraction to CO . While our calculation does not include photo-chemical effects and assumes the isothermal structure, we have checked that our calculated altitude for GJ1214b is similar with that from Morley et al. (2013). The calculated pressures at that altitude for WASP-80b are approximately 1×10^{-4} bar and 1×10^{-2} bar for temperatures, T , of 600 K and 800 K, respectively. Thus, we assume that $P_{\text{top}} = 1 \times 10^{-5}$ bar and $P_{\text{bot}} = 1 \times 10^{-3}$ bar for $T = 600$ K and that $P_{\text{top}} = 1 \times 10^{-3}$ bar and $P_{\text{bot}} = 0.1$ bar for $T = 800$ K.

As for the particle size, we assume $a_{\text{haze}} = 0.04 \text{ }\mu\text{m}$, which is the typical size of haze particles

observed in Titan’s atmosphere (Tomasko et al. 2009). Larger particles with $a_{\text{haze}} \gtrsim 0.1 \mu\text{m}$ would be incompatible with the spectral feature such that the transit radius is larger in the optical region than in the NIR region. For $a_{\text{haze}} \lesssim 0.1 \mu\text{m}$, the Rayleigh scattering by haze particles determines the spectrum in the optical region. For an appropriate choice of n_{haze} , the Rayleigh slope would be consistent with the spectral feature that we have observed. Because different sets of a_{haze} and n_{haze} yield similar spectral features, we regard n_{haze} as a free parameter in this study. The number density n_{haze} is assumed to be between 10 cm^{-3} and $1 \times 10^6 \text{ cm}^{-3}$, which is an expected range in Titan’s atmosphere (Liang et al. 2007) and hydrogen-rich atmospheres of warm exoplanets (e.g. Morley et al. 2013), although its exact value is uncertain.

We thank L. Mancini for kindly providing filter information. A. F. thanks M. Kuzuhara for meaningful discussion about atmospheric study of gas giants. Y. K. and M. I. thank N. Iwagami and Y. Ito for fruitful discussion about modeling of the transmission spectra. This work is partially supported by Optical & Near-Infrared Astronomy Inter-University Cooperation Program from the Ministry of Education, Culture, Sports, Science and Technology of Japan (MEXT). N. N. acknowledges supports by NAOJ Fellowship, Inoue Science Research Award, and Grant-in-Aid for Scientific Research (A) (No. 25247026) from the MEXT. S. N. and M. T. are supported by Japan Society for the Promotion of Science (JSPS) Grant-in-Aid: Young Scientists (A) (No. 25707012) and No. 22000005, respectively. Y. H. and K. K. are supported by Grant-in-Aid for JSPS Fellows: No. 25000465 and No. 2611515, respectively.

REFERENCES

- Barman, T. 2007, *ApJ*, 661, L191
- Barros, S. C. C., Boué, G., Gibson, N. P., Pollacco, D. L., Santerne, A., Keenan, F. P., Skillen, I., & Street, R. A. 2013, *MNRAS*, 430, 3032
- Chase, M. W. 1998, NIST-JANAF Thermochemical Tables (the American Chemical Society and the American Institute of Physics for the National Institute of Standards and Technology)
- Claret, A., Hauschildt, P. H., & Witte, S. 2012, *A&A*, 546, A14
- Eastman, J., Siverd, R., & Gaudi, B. S. 2010, *PASP*, 122, 935
- Fortney, J. J. 2005, *MNRAS*, 364, 649
- Fortney, J. J., Mordasini, C., Nettelmann, N., Kempton, E. M.-R., Greene, T. P., & Zahnle, K. 2013, *ApJ*, 775, 80
- Fukui, A., et al. 2011, *PASJ*, 63, 287
- . 2013, *ApJ*, 770, 95

- Gibson, N. P., Aigrain, S., Barstow, J. K., Evans, T. M., Fletcher, L. N., & Irwin, P. G. J. 2013, MNRAS, 436, 2974
- Gibson, N. P., Pont, F., & Aigrain, S. 2011, MNRAS, 411, 2199
- Goody, R. M., & Yung, Y. L. 1989, Atmospheric Radiation. Theoretical Basis (Oxford University Press)
- Grillmair, C. J., et al. 2008, Nature, 456, 767
- Holman, M. J., et al. 2010, Science, 330, 51
- Howe, A. R., & Burrows, A. S. 2012, ApJ, 756, 176
- Hoyer, S., Rojo, P., & López-Morales, M. 2012, ApJ, 748, 22
- Johnson, J. A., et al. 2012, AJ, 143, 111
- Khare, B. N., Sagan, C., Arakawa, E. T., Suits, F., Callcott, T. A., & Williams, M. W. 1984, Icarus, 60, 127
- Knutson, H. A., Benneke, B., Deming, D., & Homeier, D. 2014a, Nature, 505, 66
- Knutson, H. A., et al. 2014b, ApJ, 785, 126
- Kotani, T., et al. 2005, Nuovo Cimento C Geophysics Space Physics C, 28, 755
- Kreidberg, L., et al. 2014, Nature, 505, 69
- Kurosaki, K., Ikoma, M., & Hori, Y. 2014, A&A, 562, A80
- Kurucz, R. L. 1992, Rev. Mexicana Astron. Astrofis., 23, 45
- Kuzuhara, M., et al. 2013, ApJ, 774, 11
- Liang, M.-C., Yung, Y. L., & Shemansky, D. E. 2007, ApJ, 661, L199
- Lodders, K. 2003, ApJ, 591, 1220
- Maciejewski, G., et al. 2013, AJ, 146, 147
- Madhusudhan, N. 2012, ApJ, 758, 36
- Mancini, L., et al. 2014, A&A, 562, A126
- Mandel, K., & Agol, E. 2002, ApJ, 580, L171
- Mazeh, T., et al. 2013, ApJS, 208, 16
- Miller-Ricci, E., & Fortney, J. J. 2010, ApJ, 716, L74

- Morley, C. V., Fortney, J. J., Kempton, E. M.-R., Marley, M. S., Visscher, C., & Zahnle, K. 2013, *ApJ*, 775, 33
- Nagayama, T., et al. 2003, in *Society of Photo-Optical Instrumentation Engineers (SPIE) Conference Series*, Vol. 4841, *Instrument Design and Performance for Optical/Infrared Ground-based Telescopes*, ed. M. Iye & A. F. M. Moorwood, 459–464
- Narita, N., Nagayama, T., Suenaga, T., Fukui, A., Ikoma, M., Nakajima, Y., Nishiyama, S., & Tamura, M. 2013, *PASJ*, 65, 27
- Narita, N., et al. 2007, *PASJ*, 59, 763
- Nikolov, N., et al. 2014, *MNRAS*, 437, 46
- Öberg, K. I., Murray-Clay, R., & Bergin, E. A. 2011, *ApJ*, 743, L16
- Ohta, Y., Taruya, A., & Suto, Y. 2009, *ApJ*, 690, 1
- Pont, F., Knutson, H., Gilliland, R. L., Moutou, C., & Charbonneau, D. 2008, *MNRAS*, 385, 109
- Press, W. H., Teukolsky, S. A., Vetterling, W. T., & Flannery, B. P. 1992, *Numerical recipes in C. The art of scientific computing*, ed. Press, W. H., Teukolsky, S. A., Vetterling, W. T., & Flannery, B. P.
- Rothman, L. S., et al. 2013, *J. Quant. Spec. Radiat. Transf.*, 130, 4
- Schwarz, G. 1978, *Ann. Statistics*, 6, 461
- Sing, D. K., Désert, J.-M., Lecavelier Des Etangs, A., Ballester, G. E., Vidal-Madjar, A., Parmentier, V., Hebrard, G., & Henry, G. W. 2009, *A&A*, 505, 891
- Sing, D. K., et al. 2013, *MNRAS*, 436, 2956
- Snellen, I. A. G., de Kok, R. J., de Mooij, E. J. W., & Albrecht, S. 2010, *Nature*, 465, 1049
- Southworth, J., Bruni, I., Mancini, L., & Gregorio, J. 2012, *MNRAS*, 420, 2580
- Steffen, J. H., et al. 2012, *Proceedings of the National Academy of Science*, 109, 7982
- Swain, M. R., Line, M. R., & Deroo, P. 2014, *ApJ*, 784, 133
- Swain, M. R., Vasisht, G., & Tinetti, G. 2008, *Nature*, 452, 329
- Swain, M. R., et al. 2009, *ApJ*, 704, 1616
- . 2010, *Nature*, 463, 637
- Tinetti, G., Deroo, P., Swain, M. R., Griffith, C. A., Vasisht, G., Brown, L. R., Burke, C., & McCullough, P. 2010, *ApJ*, 712, L139

- Tinetti, G., et al. 2007, *Nature*, 448, 169
- Tomasko, M. G., Doose, L. R., Dafoe, L. E., & See, C. 2009, *Icarus*, 204, 271
- Triaud, A. H. M. J., et al. 2013, *A&A*, 551, A80
- Wakeford, H. R., et al. 2013, *MNRAS*, 435, 3481
- Winn, J. N., et al. 2008, *ApJ*, 683, 1076
- Yanagisawa, K., Kuroda, D., Yoshida, M., Shimizu, Y., Nagayama, S., Toda, H., Ohta, K., & Kawai, N. 2010, in *American Institute of Physics Conference Series*, Vol. 1279, American Institute of Physics Conference Series, ed. N. Kawai & S. Nagataki, 466–468
- Yanagisawa, K., et al. 2006, in *Society of Photo-Optical Instrumentation Engineers (SPIE) Conference Series*, Vol. 6269, Society of Photo-Optical Instrumentation Engineers (SPIE) Conference Series
- Yanagisawa, K., et al. 2008, in *Society of Photo-Optical Instrumentation Engineers (SPIE) Conference Series*, Vol. 7014, Society of Photo-Optical Instrumentation Engineers (SPIE) Conference Series

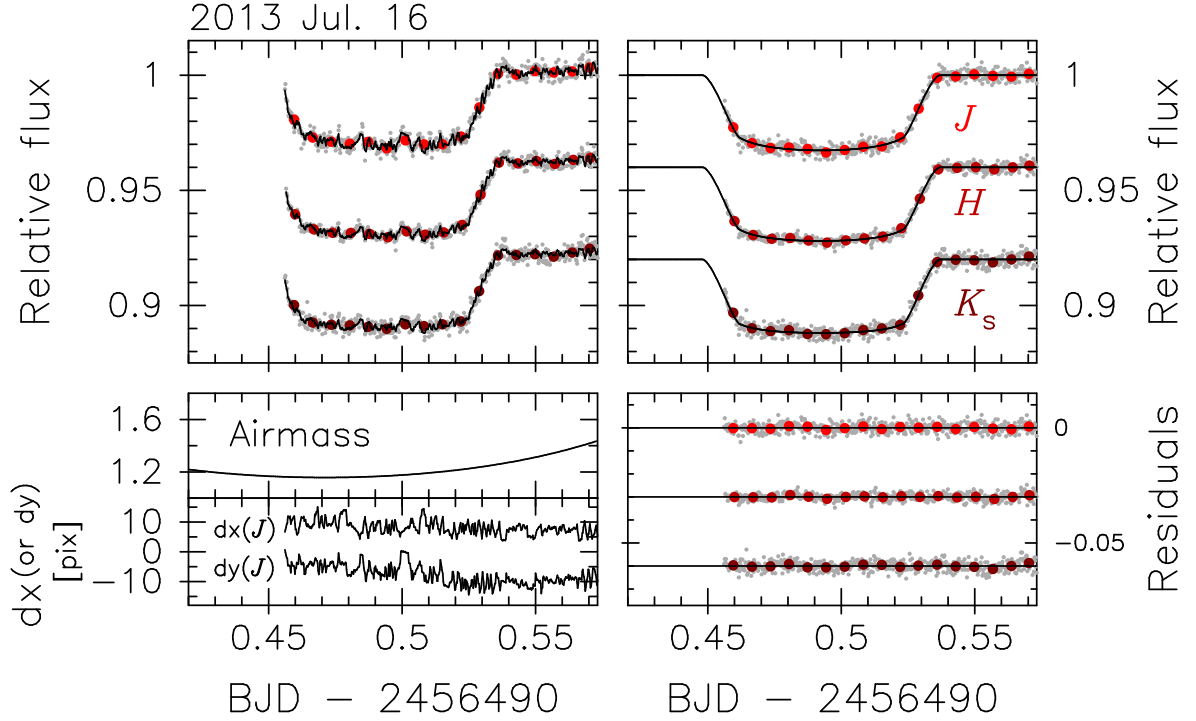


Fig. 1.— (Left upper) Baseline-uncorrected transit light curves of WASP-80b observed with IRSF/SIRIUS on 2013 July 16. The J -, H -, and K_s -band light curves are shown from top to bottom, where the lower two are arbitrary shifted along the vertical direction for display. The small gray points and large colored points are un-binned and 10-minute binned data, respectively. The solid lines are the best-fit transit+baseline models derived from the MCMC analysis. (Left lower) The air mass change (top), and the stellar positional changes in x and y directions on the J -band detector, where arbitrary constant values are added for clarity (bottom). (Right upper) Baseline-corrected light curves. (Right lower) Residual light curves.

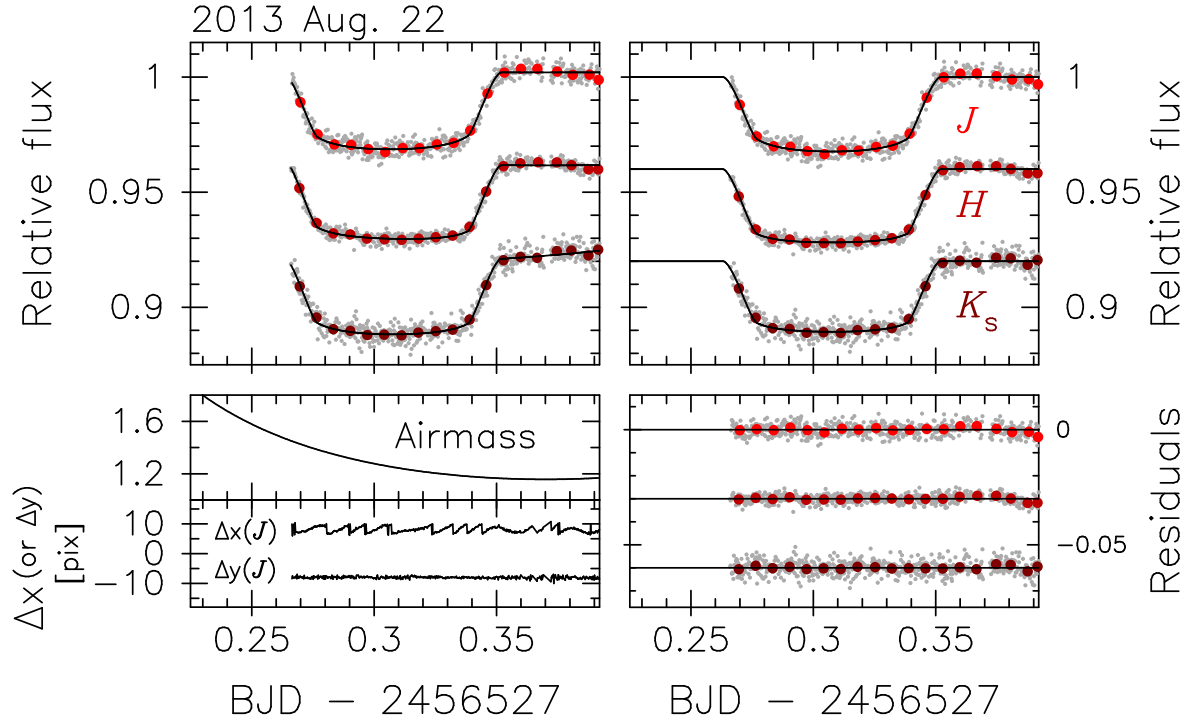


Fig. 2.— Same as Figure 1, but for the data obtained on 2013 August 22.

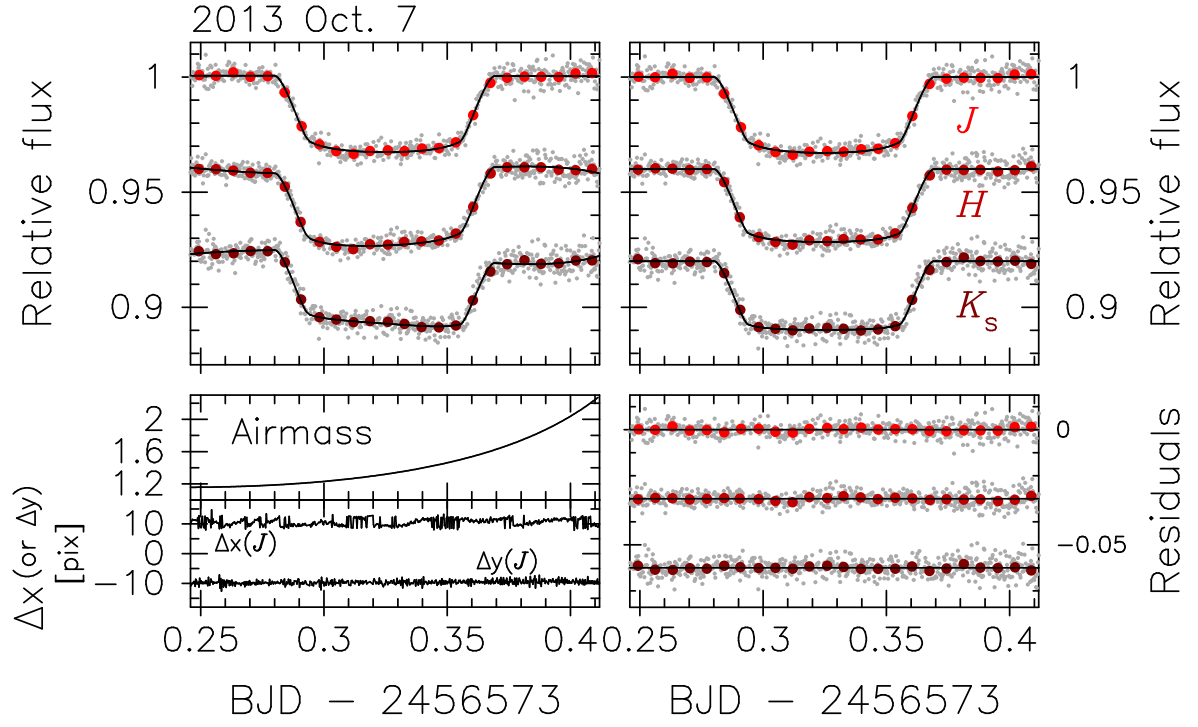


Fig. 3.— Same as Figure 1, but for the data obtained on 2013 October 7.

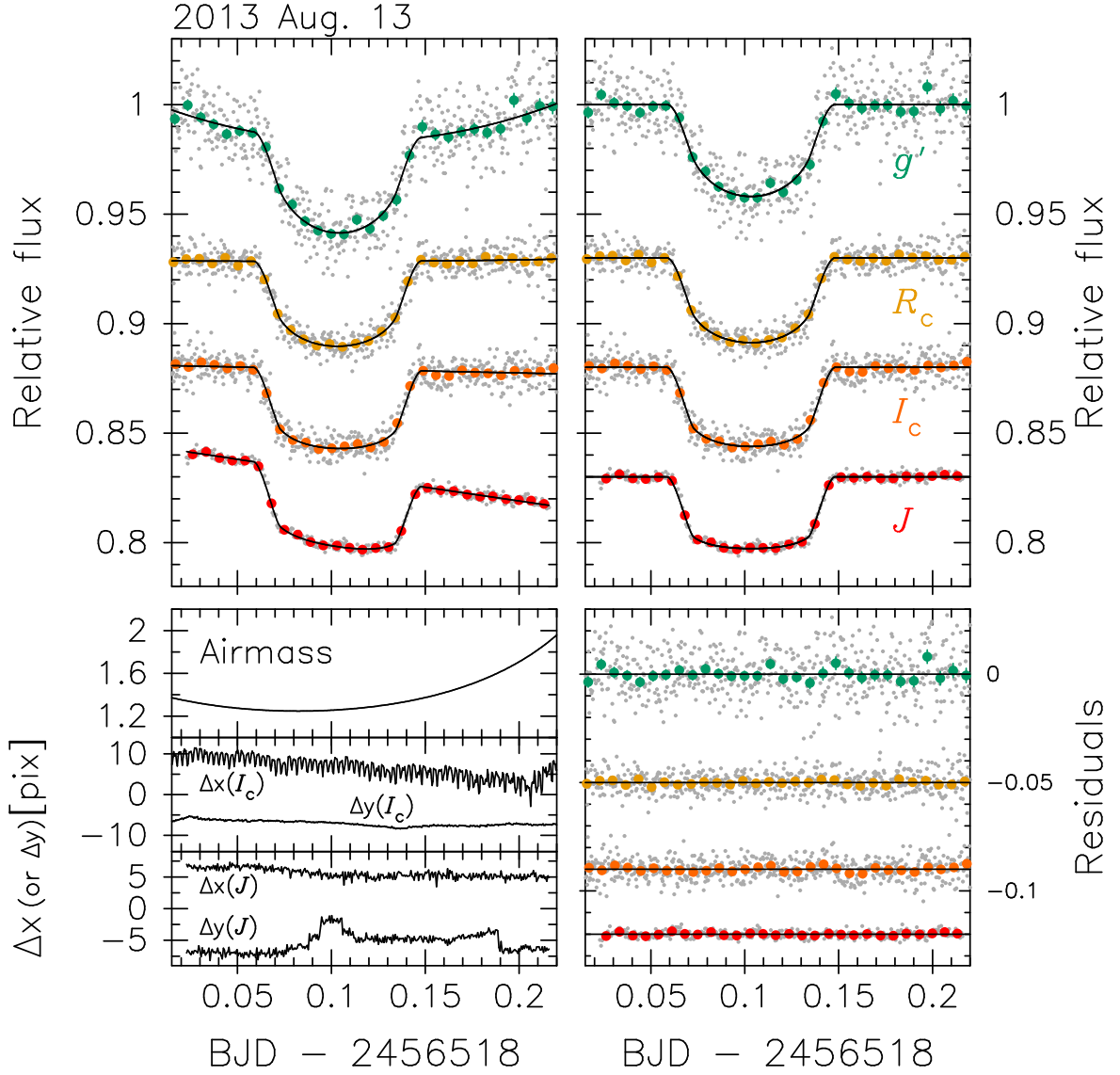


Fig. 4.— (Left upper) Baseline-uncorrected transit light curves of WASP-80b observed at OAO on 2013 August 13. The g' -, R_c -, I_c -, and J -band light curves are shown from top to bottom, where the lower three are arbitrarily shifted along the vertical direction for display. The other meanings are the same as in Figure 1. (Left lower) The air mass change (top), and the stellar positional changes in x and y directions on the MITSuME/ I_c -band detector (middle) and those on the ISLE/ J -band detector (bottom), where arbitral constant values are added for clarity. (Right upper) Baseline-corrected light curves. (Right lower) Residual light curves.

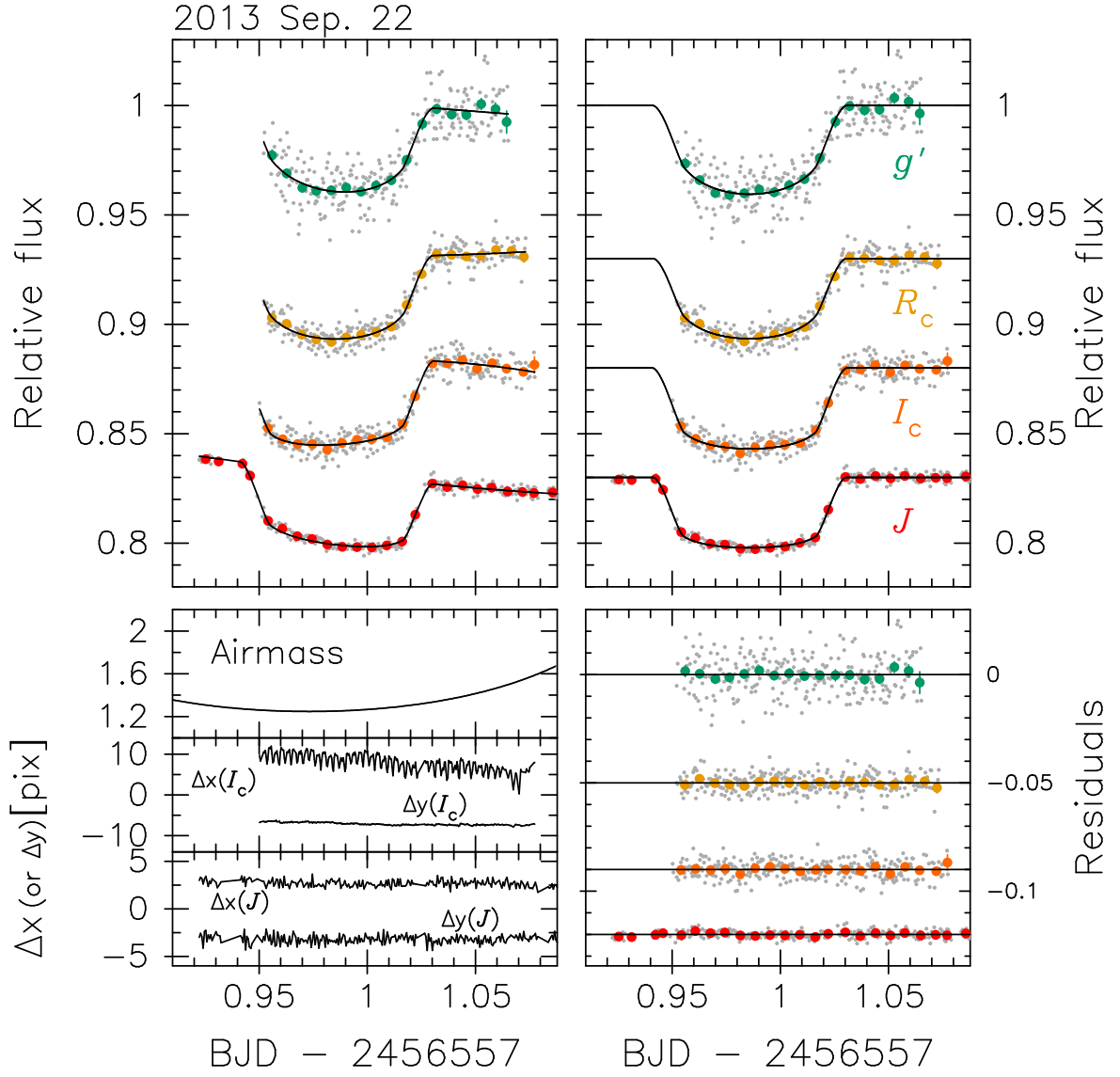


Fig. 5.— Same as Figure 4, but for the data obtained on 2013 September 22.

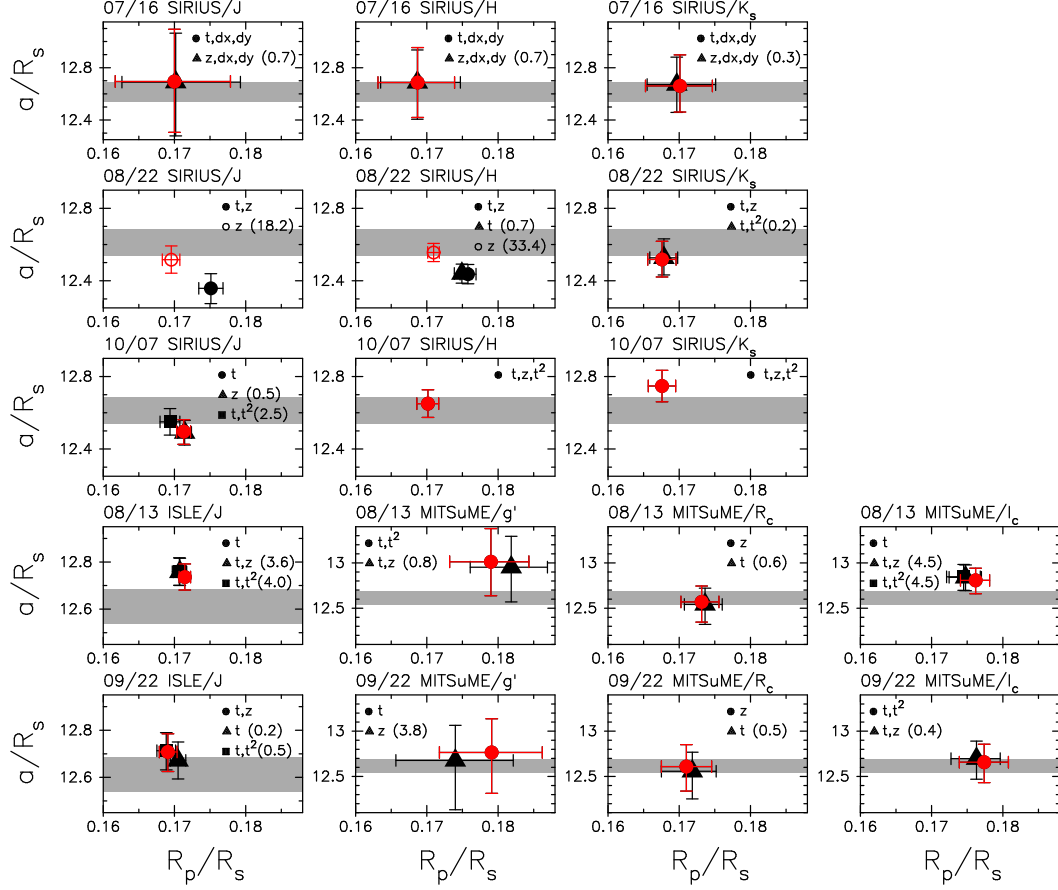


Fig. 6.— Comparison of R_p/R_s and a/R_s derived by the AMOEBA fitting for each light curve using different baseline models. The results for each light curve are shown in each panel, on top of which the observing month/day and instrument/filter are indicated. The filled circle, triangle, and square denote the values derived by using the baseline models that give the minimum, second-minimum, and third-minimum BIC values, respectively. The number in parenthesis in legend indicates ΔBIC with respect to the minimum BIC value. Note only the plots giving $\Delta\text{BIC} < 5$ are shown in this Figure, except for the panels for SIRIUS/*J* and *H* on August 22, where the values derived from $\{X\} = \{t\}$ are additionally shown as open circles. The gray belt indicates the $1\text{-}\sigma$ credible region of a/R_s derived by Mancini et al. (2014). Our choices for the best-describing baseline models are indicated by red color.

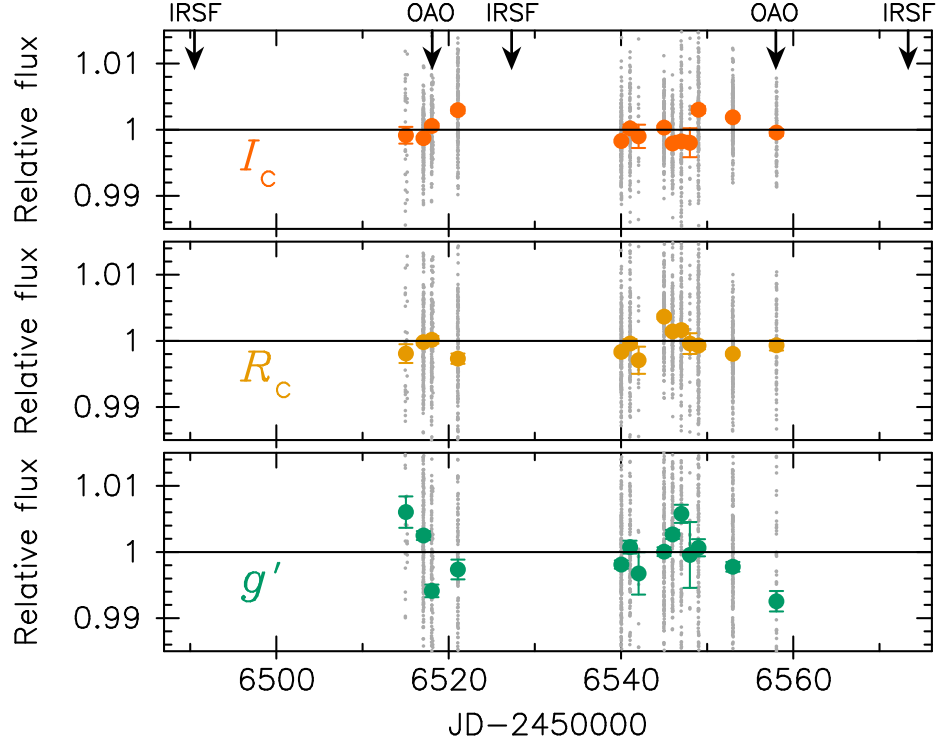


Fig. 7.— The 43-days-long light curves of WASP-80 observed with the MITSuME telescope in I_c , R_c , and g' bands (top, middle, and bottom panels, respectively). The gray dots are un-binned data points excluding the ones that fall in any transits, whereas the large points indicate nightly-binned data. The error bars are calculated as RMS of nightly un-binned data divided by square of the number of data points. The nights when the transit observations were conducted at IRSF and OAO are indicated as arrows in the top panel.

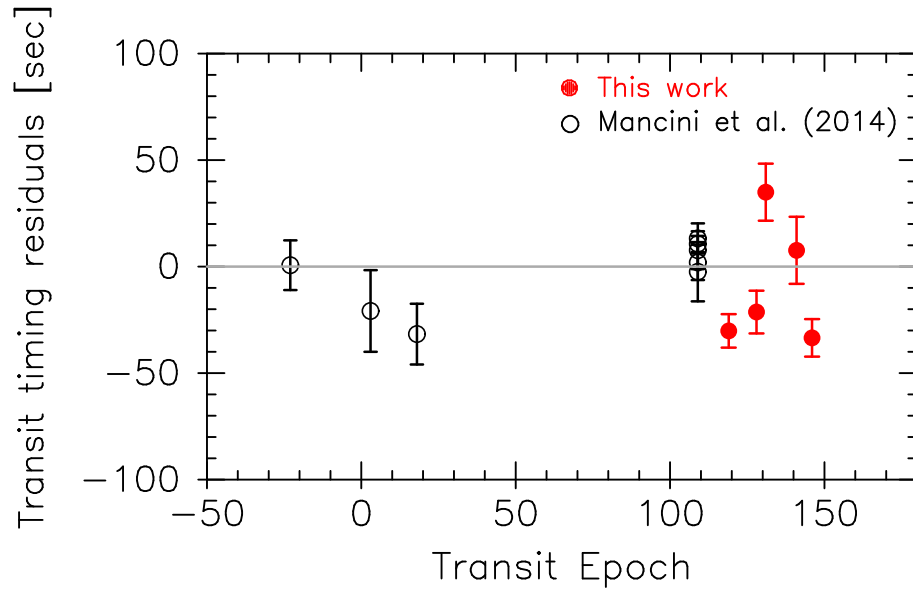


Fig. 8.— Residuals of the observed mid-transit times from the liner ephemeris calculated by fitting all the data shown here. The latest five data points are from this work, and others are from Mancini et al. (2014) including the re-analysis data of the light curves presented in Triaud et al. (2013).

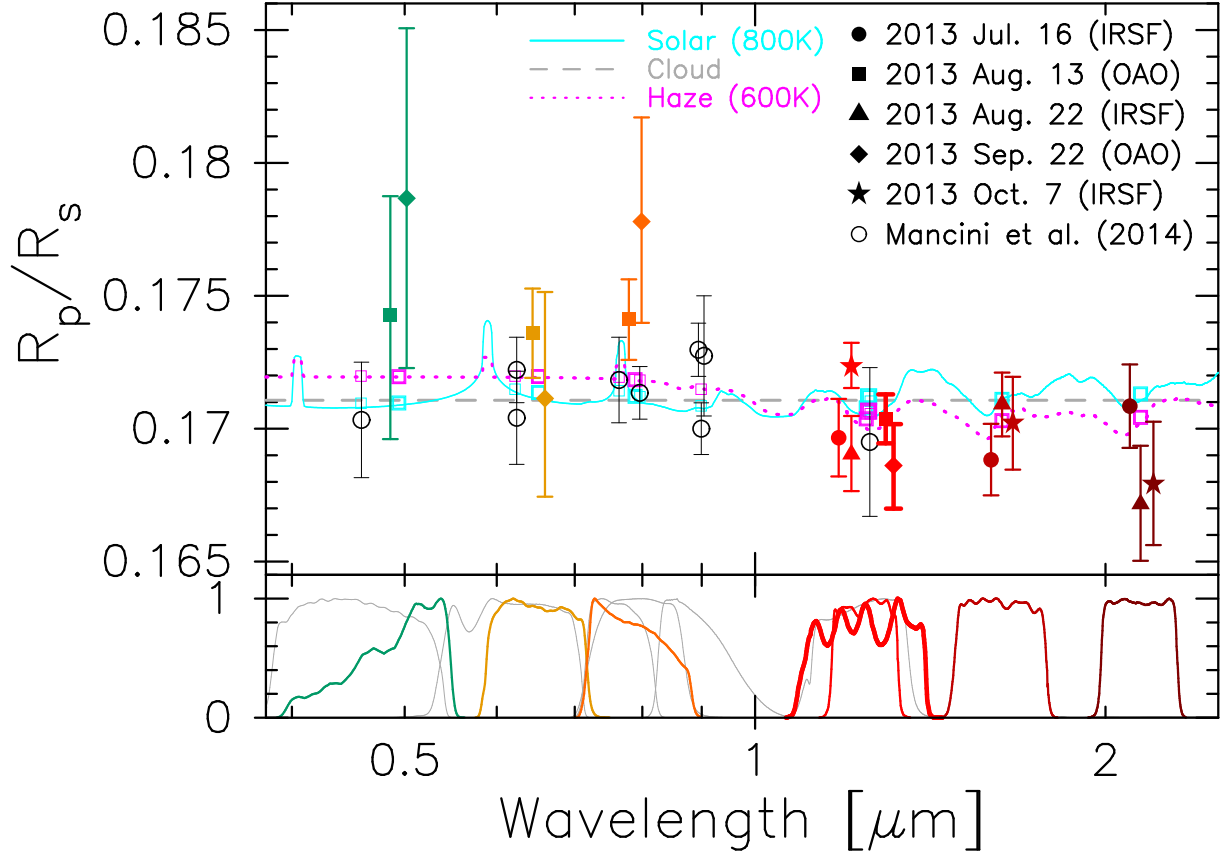


Fig. 9.— (Top) Observed and theoretical transmission spectra of WASP-80b. The R_p/R_s values obtained in this work are indicated as filled marks, where different marks are for the data obtained on different nights as indicated at the upper right in the panel. The J -band data from ISLE are indicated as bold lines for ease of recognizing. The open circles indicate the data from Mancini et al. (2014), which include re-analysis of the data presented in Triaud et al. (2013). Data points are slightly shifted in the horizontal direction for display when there are multiple observations at one band pass. The solid, dashed, and dotted lines show theoretical spectra for solar-abundance (800K), cloudy, and hazy (600K) atmospheres, respectively (see text for details). Note the theoretical spectra shown are smoothed for clarity. The open squares indicate the integrals of the theoretical spectra for the respective band passes. (Bottom) Transmission curves for the respective filters, where the bold, normal, and thin lines are for the ISLE/ J -band filter, the other filters used in this work, and those used in Mancini et al. (2014), respectively.

Table 1. Observing Log.

Date [UT]	Telescope/ Instrument	Filter	Exp. time [s]	N_{obs}^a
2013 July 16	IRSF/SIRIUS	J	10	541
	IRSF/SIRIUS	H	10	537
	IRSF/SIRIUS	K_s	10	539
2013 August 13	MITSuME 50cm	g'	30	562
	MITSuME 50cm	R_c	30	566
	MITSuME 50cm	I_c	30	563
	OA0188cm/ISLE	J	45	324
2013 August 22	IRSF/SIRIUS	J	10	566
	IRSF/SIRIUS	H	10	576
	IRSF/SIRIUS	K_s	10	582
2013 September 22	MITSuME 50cm	g'	30	268
	MITSuME 50cm	R_c	30	290
	MITSuME 50cm	I_c	30	295
	OA0188cm/ISLE	J	45	241
2013 October 7	IRSF/SIRIUS	J	15	597
	IRSF/SIRIUS	H	15	597
	IRSF/SIRIUS	K_s	15	603

^a The number of observed data points excluding outliers.

Table 2. Summary of Light Curve Preparation.

Instrument	Obs. Date [UT]	Filter	N_{comp}^a	R_{ap}^b [pixel]	$\{\mathbf{X}\}$	RMS [%]	β
SIRIUS	2013 Jul. 16	J	3	12.0	$t, \Delta x, \Delta y$	0.194	1.24
		H	3	14.0	$t, \Delta x, \Delta y$	0.145	1.58
		K_s	4	12.0	$t, \Delta x, \Delta y$	0.200	1.33
	2013 Aug. 22	J	3	9.0	z	0.251	1.36
		H	3	9.0	z	0.177	1.68
		K_s	2	9.0	t, z	0.298	1.13
	2013 Oct. 7	J	3	16.0	t	0.270	1.06
		H	2	16.0	t, z, t^2	0.265	1.17
		K_s	3	14.0	t, z, t^2	0.329	1.01
ISLE	2013 Aug. 13	J	1	20.0	t	0.164	1.35
	2013 Sep. 22	J	1	21.0	t, z	0.177	1.28
MITSuME	2013 Aug. 13	g'	8	2.5	t, t^2	1.05	1.02
		R_c	6	4.0	z	0.477	1.00
		I_c	9	3.5	t	0.491	1.01
	2013 Sep. 22	g'	8	3.0	t	0.855	1.00
		R_c	6	4.0	z	0.417	1.12
		I_c	9	3.5	t, t^2	0.404	1.08

^a The number of comparison stars.

^b Aperture radius.

Table 3. MCMC Results.^a

Parameter	Value					
	2013 Jul. 16	2013 Aug. 13	2013 Aug. 22	2013 Sep. 22	2013 Oct. 7	Mancini et al. (2014)
T_c	6490.492507	6518.10335	6527.30758	6557.98585	6573.32468	...
[BJD _{TDB} -2450000]	± 0.000091	± 0.00012	± 0.00016	± 0.00018	± 0.000088	...
u_1 (g')	...	0.842 ± 0.087	...	$0.642^{+0.095}_{-0.097}$
u_1 (R_c)	...	$0.624^{+0.042}_{-0.043}$...	$0.551^{+0.056}_{-0.059}$
u_1 (I_c)	...	$0.407^{+0.048}_{-0.050}$...	$0.353^{+0.052}_{-0.054}$
u_1 (J)	0.270 ± 0.026	0.254 ± 0.032	$0.265^{+0.035}_{-0.037}$	$0.258^{+0.038}_{-0.040}$	0.204 ± 0.027	...
u_1 (H)	0.213 ± 0.023	...	$0.126^{+0.033}_{-0.031}$...	$0.133^{+0.033}_{-0.038}$...
u_1 (K_s)	0.153 ± 0.029	...	0.159 ± 0.038	...	$0.048^{+0.048}_{-0.053}$...
R_p/R_s (g')	...	$0.1743^{+0.0045}_{-0.0047}$...	0.1787 ± 0.0064	...	0.17033 ± 0.00217
R_p/R_s (R_c)	...	0.1736 ± 0.0017	...	$0.1711^{+0.0040}_{-0.0037}$...	0.17041 ± 0.00175
R_p/R_s (I_c)	...	0.1741 ± 0.0015	...	0.1778 ± 0.0039	...	0.17183 ± 0.00161
R_p/R_s (J)	0.1697 ± 0.0015	0.1704 ± 0.00092	0.1690 ± 0.0014	0.1686 ± 0.0016	$0.17234^{+0.00089}_{-0.00081}$	0.1695 ± 0.0028
R_p/R_s (H)	0.1688 ± 0.0014	...	0.1709 ± 0.0012	...	0.1702 ± 0.0017	...
R_p/R_s (K_s)	0.1708 ± 0.0016	...	0.1672 ± 0.0022	...	0.1679 ± 0.0023	...

^a The MCMC analysis in this work is performed by fixing $i_{\text{orb}} = 88.91$ deg and $a/R_s = 12.612$, which are obtained from Mancini et al. (2014).

Table 4. Statistical Results of Model Fitting to the Transmission Spectrum.

	Solar (800K)	Cloud	Haze (800K)	Haze (600K)	Solar (600K)
<i>All Data</i>					
χ^2/dof	35.4/25	34.7/25	29.3/24	26.8/24	44.2/25
Discrepancy [σ]	1.7	1.7	1.3	1.0	2.7
<i>w/o MITSuME Data</i>					
χ^2/dof	24.3/19	22.7/19	20.2/18	19.5/18	29.7/19
Discrepancy [σ]	1.3	1.1	0.99	0.92	1.9